ADVANCED ENERGY MATERIALS
www.advenergymat.de

Co-Intercalation Batteries (CoIBs): Role of TiS_2 as Electrode for Storing Solvated Na Ions

Guillermo Alvarez Ferrero, Gustav Åvall, Katherine A. Mazzio, Youhyun Son, Knut Janßen, Sebastian Risse, and Philipp Adelhelm**

The co-intercalation of solvent molecules along with Na^+ into the crystal lattice of electrode materials is an undesired process in sodium batteries. An exception is the intercalation of ether solvated alkali ions into graphite, a fast and highly reversible process. Here, reversible co-intercalation is shown to also be possible for other layered materials, namely titanium disulfide. Operando X-ray diffraction and dilatometry are used to demonstrate different storage mechanisms for different electrolyte solvents. Diglyme is found to co-intercalate into the TiS_2 leading to a change in the voltage profile and an increase in the interlayer spacing (≈150%). This behavior is different compared to other solvents, which expand much less during Na storage (24% for tetrahydrofuran [THF] and for a carbonate mixture). For all solvents, specific capacities (2nd cycle) exceed 250 mAh g^{-1} whereas THF exhibited the best stability after 100 cycles. The solvent co-intercalation is rationalized by density functional theory and linked to the stability of the solvation shells, which is largest for diglyme. Finally, the TiS_2 electrode with diglyme electrolyte is paired with a graphite electrode to realize the first proof-of-concept solvent co-intercalation battery, that is, a battery with two electrodes that both rely on reversible co-intercalation of solvent molecules.

1. Introduction

The development of high-performance rechargeable batteries has recently attracted much attention for applications such as electric vehicles, grid energy storage, and portable electronic devices.[1] With the rising demand for lithium-ion batteries (LIBs), sodium-ion batteries (SIBs) may become an attractive alternative with the promise of improved safety, reduced cost, and lower environmental impact.[2] LIBs and SIBs rely on the same concept of shuttling Li^+ or Na^+ between two electrodes through a liquid electrolyte solution. The larger ion size of Na^+, however, has major consequences on the battery chemistry, which provides challenges and opportunities for designing electrode materials and electrolyte solutions.[3] A peculiar example is graphite, which is currently used as an anode material in most LIBs. In SIBs (using the traditional carbonate-based electrolytes) the storage behavior is poor due to unfavorable thermodynamic processes, which results in low specific capacities.[4] A strategy around this problem is to choose different solvents, especially ethers, which can co-intercalate into the graphite structure forming ternary graphite intercalation compounds.[5] Although the co-intercalation of solvent molecules leads to a large increase in the graphene interlayer spacing, the cycle life and rate capability of the reaction are excellent. Several thousand cycles can be obtained without any notable capacity loss.[6] Despite this, evidence for a comparable reaction with other electrode materials is largely lacking so far. Particularly interesting would be to identify a cathode material that operates via the same mechanism. Designing a battery based on solvent co-intercalation at both electrodes could be appealing as, due to the absence of desolvation steps, the charge-transfer resistances in the battery can be minimized. It has been shown that stripping of the solvation shell can be the rate limiting step for battery operation, especially at subzero temperatures.[7] Such a solvent co-intercalation battery (CoIB) could therefore be more energy efficient compared to other batteries or could enable a better low-temperature performance.

Transition metal dichalcogenides (TMDs) have emerged as promising electrode materials owing to their low cost, high electrical conductivity, good thermal stability, and environmental friendliness.[8] In addition, different reaction mechanisms, such as insertion or conversion processes, have been explored within their layered structures.[8c] Among them, titanium disulfide (TiS_2) and its 2D framework, offer several advantages as active electrode materials, including a high conductivity (compared

G. Alvarez Ferrero, G. Åvall, K. A. Mazzio, Y. Son, K. Janßen, P. Adelhelm
Institut für Chemie
Humboldt-Universität zu Berlin
12489 Berlin, Germany
E-mail: guillermo.alvarez.ferrero@hu-berlin.de;
philipp.adelhelm@hu-berlin.de
K. A. Mazzio, S. Risse, P. Adelhelm
Joint research group Operando Battery Analysis (CE-GOBA)
Helmholtz-Zentrum Berlin
14109 Berlin, Germany
S. Risse
Electrochemical Energy Storage
Helmholtz-Zentrum Berlin
14109 Berlin, Germany

The ORCID identification number(s) for the author(s) of this article can be found under https://doi.org/10.1002/aenm.202202377.

DOI: 10.1002/aenm.202202377

to metal oxides),[9] a larger interlayer distance (5.69 Å) relative to graphite (3.35 Å),[8c] and high structural and chemical stability.[10] Due to these features, TiS_2 has regained attention as an electrode material for different types of batteries, ranging from lithium[11] to potassium,[12] and also for multivalent cations such as calcium[13] and magnesium.[13,14]

Several papers on the use of TiS_2 as an electrode material for SIBs have been published, all of which demonstrate that the voltage profiles and electrochemical behavior are highly dependent on the type of electrolyte used. Yet, this has seldom been explicitly stated, nor has the cause of the electrolyte dependence been investigated.[10,15] Ryu et al. reported on the Na storage properties of TiS_2 using a 1 M electrolyte solution of sodium trifluoromethanesulfonate (NaOTf) in tetraethyleneglycol dimethylether (tetraglyme, 4G). They observed a two-plateau voltage profile where the first plateau was ascribed to a conversion reaction (≈2.1 V) and the second to an intercalation reaction (≈1.6 V),[9] where the low reported cyclability was attributed to the formation of a Na_xTiS_2 intermediate at around 1.55 V versus Na^+/Na. The ex situ X-ray diffraction (XRD) analysis showed that the TiS_2 (001) peak disappears at 0.8 V, before recovering its initial status in the desodiated state. The above plateaus were also observed when carbonate solvents were used,[10a] however, they are less defined compared to those obtained with 4G. It is worth mentioning that the XRD peaks corresponding to TiS_2 never disappeared during their operando measurements. On the contrary, with a similar electrolyte, the TiS_2 nanoplatelets reported by Liu et al. displayed a progressive shift of the (001) peak and an attenuation of its intensity.[15c] Interestingly, when the electrolyte solvent was diethylene glycol dimethyl ether (diglyme, 2G), the voltage profile exhibited a different shape. In this case, the first plateau that normally appears at around 2.1 V is less intense and arises at a lower potential of 1.7 V.[15a] The authors ascribed the electrochemical behavior to the insertion of Na^+ into TiS_2 at around 1.5 V, followed by a conversion reaction at around 1 V to form Na_2S and $Ti_{0.77}S$, which provides additional capacity to the system. Differences between electrolyte solutions were also observed by Hu et al. who found better cycle life for 4G compared to an ethylene carbonate/diethyl carbonate (EC:DEC) mixture.[15b] Furthermore, by operando XRD, the expansion of the (001) layer distance was detected alongside the appearance of new peaks located at 12.5° and 14.5° (2θ). Similar peaks were also detected by previous authors, although they were assigned to different Na_xTiS_2 phases.[9,10]

Taking these results together it becomes clear that the sodium storage mechanism of TiS_2 electrodes depends on the electrolyte solvent. Herein, we demonstrate that the primary origin of those differences is due to co-intercalation of solvent molecules in the case of glyme-based electrolytes. These findings are related to studies on Li intercalation into TiS_2 from the early 1980s by Dahn et al., who showed by XRD the irreversible (electro-)chemical co-intercalation of propylene carbonate (PC), as well as by Whittingham, who summarized the use of different solvents for intercalating TMDs (e.g., dimethyl sulfoxide (DMSO) and formamide in the case of TiS_2).[16] In view of these early studies on the Li-TiS_2 system and more recent findings on the sodium-graphite system,[17] studying co-intercalation of solvent molecules has received some attention lately. Solvent co-intercalation is, however, still a largely unexplored strategy for tailoring the properties of electrode reactions for metal-ion batteries. In addition to operando XRD experiments, the present study also includes results from operando electrochemical dilatometry (which measures the change in electrode thickness during cycling),[18] and computational studies using density functional theory (DFT) in order to validate our findings. Furthermore, the long-term stability was also investigated to understand the structural changes that occur when cycling the TiS_2 electrodes in different electrolyte solutions. In this regard it was demonstrated that the electrochemical mechanism can be modified by tuning the electrolyte solvent. Finally, the first solvent co-intercalation battery (CoIB) was assembled with two electrodes that operate according to a reversible co-intercalation reaction.

2. Results and Discussion

2.1. Charge–Discharge Behavior for Different Electrolytes

The influence of the electrolyte composition on the Na storage in TiS_2 electrodes was studied using three different electrolytes: 1 M $NaPF_6$ in 2G, THF, and a mixture of carbonates (EC:DEC (1:1 vol%)). Differences can be observed from the galvanostatic charge–discharge experiments as shown in **Figure 1**a (2nd cycle). In agreement with previous results, the TiS_2 electrodes show a multistep behavior.[10a,15b,19] However, the voltage profile for the 2G electrolyte is clearly different from the others, showing two plateaus at 1.75 V versus Na^+/Na and 1.55 V versus Na^+/Na compared to ≈2.1 V versus Na^+/Na and 1.55 V versus Na^+/Na for THF and EC:DEC, respectively. For the latter electrolytes, an additional small plateau appears at ≈2 V versus Na^+/Na that is followed by an extended sloping region. Data for the first five cycles are shown in Figure S1, Supporting Information, which also confirm that differences between the electrolytes are observed over cycling, giving a clear indication that a different reaction mechanism occurs in the case of 2G. The combined overpotentials for the reaction can be seen from Figure 1b, which shows charge/discharge curves for the 1st and 5th cycles plotted as hysteresis. The smallest gap is found in the case of THF (a cyclic ether) which indicates the best kinetic behavior among the different electrolytes. This is in line with the reversible storage capacity which is slightly higher (280 mAh g^{-1}, 5th cycle) compared to the other electrolytes (245 mAh g^{-1} for 2G and 260 mAh g^{-1} for EC:DEC). Another difference between the cells is found for the initial Coulomb efficiency (ICE) which was lower when 2G was used as solvent (65% vs 91% for THF and 88% for EC:DEC) suggesting that an additional (irreversible) reaction takes place, as can be clearly seen in Figure S1a, Supporting Information. In this regard, it has to be mentioned that the tail-like feature observed in Figure 1b and Figure S1, Supporting Information, at low voltages on the first cycle is due to the conductive carbon additive of the electrode (see Figure S2, Supporting Information). Irreversible processes linked to the carbon additive should be more or less comparable for all electrolyte formulations yet the ICE value in the case of 2G is lower compared to THF and EC:DEC. As it is known that 2G is stable within the applied voltage window,[4a] the additional reaction must be linked to a specific reaction between 2G and the TiS_2 electrode.

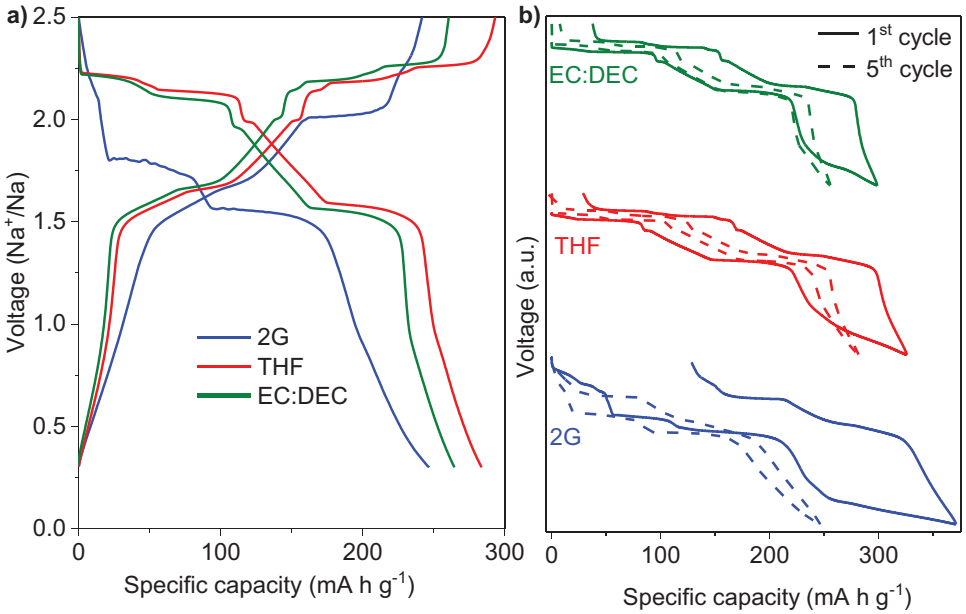

Figure 1. Galvanostatic sodiation and desodiation potential profiles for titanium disulfide electrodes with different electrolyte solvents at a) 10 mA g^{-1} for the 2nd cycle and b) comparison of the hysteresis plot between the 1st and 5th cycle. The different electrolytes employed are 1 M $NaPF_6$ in 2G, THF, and EC:DEC.

2.2. Structural Analysis

Operando XRD was performed to gain insight into the structural evolution that occurred alongside the observed differences in the electrochemical behavior (see Figure S3, Supporting Information, for a scheme of the operando XRD cell). The XRD patterns of the TiS_2 electrodes cycled in THF- and 2G-based electrolytes are presented in **Figures 2** and **3**, respectively (properties of the pristine electrode in reflection geometry are shown in the Supporting Information, see Figure S4a, Supporting Information). All operando measurements were performed in transmission geometry, which results in relatively weak (00*l*) peaks for TiS_2 (the (001) peak is located at 15.6° (2θ), and higher order features are not discernable in the transmission patterns) due to a strong degree of preferred orientation. Similarly, the preferred orientation also significantly increases the intensity of the observed (*h*0*l*) features (see discussion in Supplementary Information). Initially, TiS_2 has its standard configuration with a $P\bar{3}m1$ space group (ICSD 52195) that is characterized as a layered structure consisting of hexagonally close packed sulfur atoms sandwiching a layer of titanium atoms. These layers are separated by a van der Waals (VDW) gap in which cations can be intercalated during reduction, see Figure 2 (Na^+ intercalation from a THF electrolyte).[20] At the same time, there is an expansion in the c-direction of the lattice and a corresponding change in crystal structure. This is clearly observed by a shift in the (001) peak from 15.6° (2θ) at OCV to 13.9° (2θ), which corresponds to the (003) feature of $Na_{0.3}TiS_2$ with an $R\bar{3}$mH space group (ICSD 201394) (purple lines, Figure 2a). The development of $Na_{0.3}TiS_2$ is further supported by the splitting pattern near the original (101) feature from TiS_2 at 34.3° (2θ). As sodiation progresses, the intensity of the (101) feature diminishes. The splitting is consistent with the formation of the (10$\bar{5}$) and (10$\bar{8}$) reflections from $Na_{0.3}TiS_2$. These features persist until the end of the voltage plateau at 2.00 V versus Na^+/Na. As soon as this plateau ends, there is a clear change in crystal structure (orange lines, Figure 2a) that is consistent with the development of $Na_{0.55}TiS_2$ with an R3mH space group (ICSD 71092). This point shows the largest change in the c-direction with a shift to 12.7° (2θ), which corresponds to the (003) reflection. Thus, this intercalation process leads to a lattice expansion of +24%. The development of this crystal structure is further supported by the new features that arise at 31.1° and 36.9° (2θ) that correspond to the (10$\bar{2}$) and (1$\bar{1}$2) reflections and the (10$\bar{5}$) and (1$\bar{1}$5) reflections, respectively. There are two contributions to each reflection due to symmetry. After the second voltage plateau, further sodiation (green patterns, Figure 2a) results in the formation of $NaTiS_2$ with an $R\bar{3}$mH space group (ICSD 26305). This results in a slight contraction in the c-direction, as signified by the (003) reflection showing up at 12.9° (2θ). The (104) reflection also arises at 34.2° (2θ), along with the (107) and (10$\bar{8}$) features at 43.1° (2θ) and 46.7° (2θ), respectively. A schematic of the observed changes in crystal structure at the different voltages is presented in Figure 2b. This is what could be considered the typical process for the sodiation of layered TiS_2.[9,10,15b,c] We find that the process is rather reversible upon desodiation, although that the desodiation process is incomplete (as already mentioned in the charge/discharge section). This is clear from the final diffraction patterns that are reported at 2 V versus Na^+/Na in the desodiated state that are consistent with contributions from a mixture of $Na_{0.55}TiS_2$ and $Na_{0.3}TiS_2$ phases. Thus, the initial TiS_2 state is not recovered after the first cycle, and the residual Na that remains in the observed Na_xTiS_2 phases is reflected in the ICE value of 91%. The modification of the structure was further confirmed from SEM images where the layered structure appeared opened (see Figure S5, Supporting

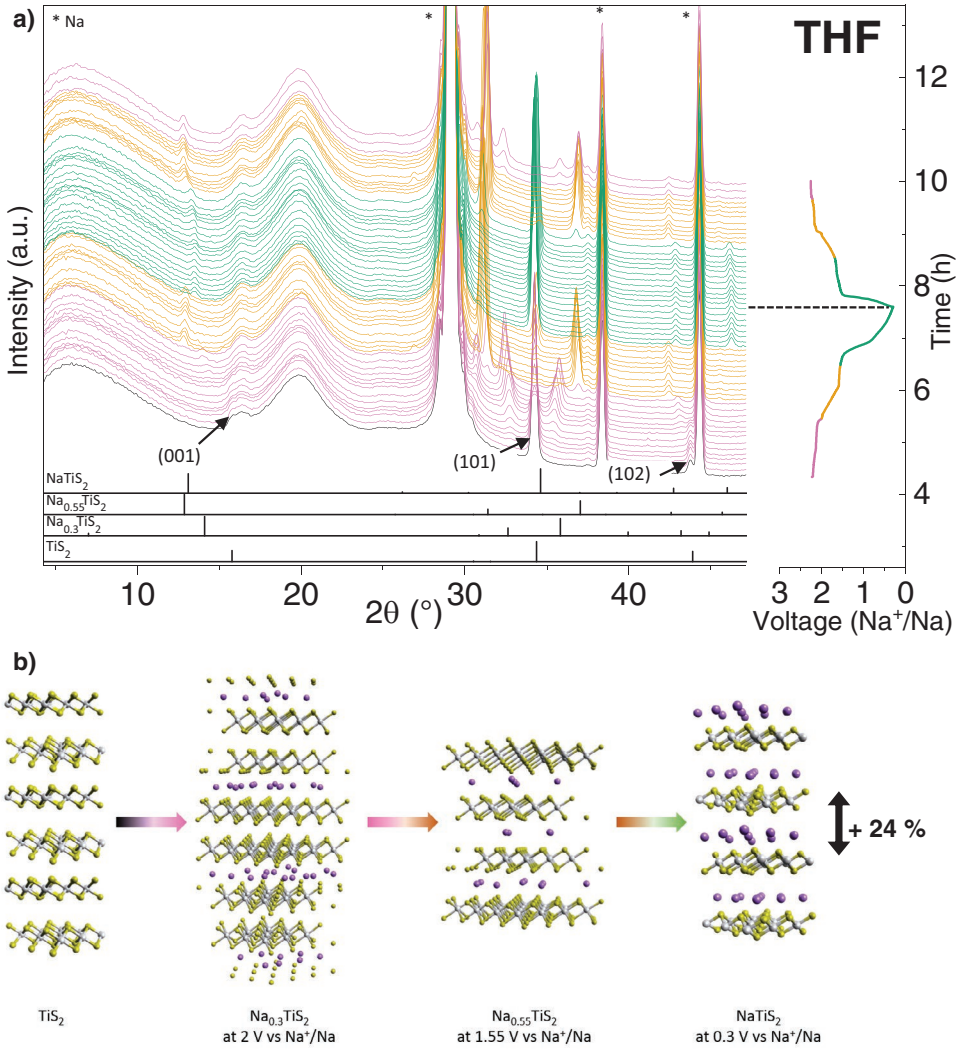

Figure 2. a) Voltage profiles at 100 mA g^{-1} with the corresponding operando diffraction patterns of the TiS_2 electrodes and the XRD patterns of standard data of $NaTiS_2$ (ICSD 26305), $Na_{0.55}TiS_2$ (ICSD 71092), $Na_{0.3}TiS_2$ (ICSD 201394), and TiS_2 (ICSD 52195); and b) schematic illustration of the mechanism during the sodium sodiation process in 1 M $NaPF_6$ in THF.

Information). It should also be mentioned that the electrodes displayed a rough and uneven surface. A comparable behavior was observed when EC:DEC was used as the solvent electrolyte (see Figures S6 and S7, Supporting Information). However, it has to be mentioned that the system is not as reversible as in the case of THF where the first sodiated phase is not visible in the desodiated state. Overall, the results indicate that in the case of THF- or EC:DEC-based electrolytes, the intercalation process follows the conventional mechanism, that is, the solvation shell is stripped during charge transfer. This is also in line with findings by Houdeville et al. for lithium intercalation from EC:DEC electrolyte solutions.[21] For diglyme electrolytes, however, the intercalation process changes and solvent co-intercalation takes place.

The operando XRD results for 2G are shown in Figure 3a. The OCV state (black lines) compares well with the other electrolyte formulations, which indicates that solvent co-intercalation does not occur simply by exposing the electrode to the electrolyte solution. In this regard, the variation of the OCV versus time remained largely constant over 4 h after the cell was assembled, demonstrating that the co-intercalation does not occur without an electrochemical driving force (see Figure S8, Supporting Information). With the onset of sodiation, during the first small voltage plateau at 2.25 V versus Na^+/Na, there is a shift in the (001) feature of TiS_2 from 15.5° to 6.1° (2θ). At the same time, new features also arise at 30.4°, 32°, and 34.5° (2θ). We also performed ex situ XRD measurements in Bragg-Brentano (reflection) geometry in order to observe changes out of plane from the transmission measurements, and found that we were able to observe not only the (001) feature, but also higher order reflections, as shown in Figure S9, Supporting Information, and related discussion. We hypothesized that this could be related to a co-intercalation process in the case of 2G that is not observed when using THF or EC:DEC. To test this hypothesis, we performed a Le Bail refinement on patterns showing this structure, and assuming an expanded $P\bar{3}m1$ space group (similar to the parent TiS_2, but with greater

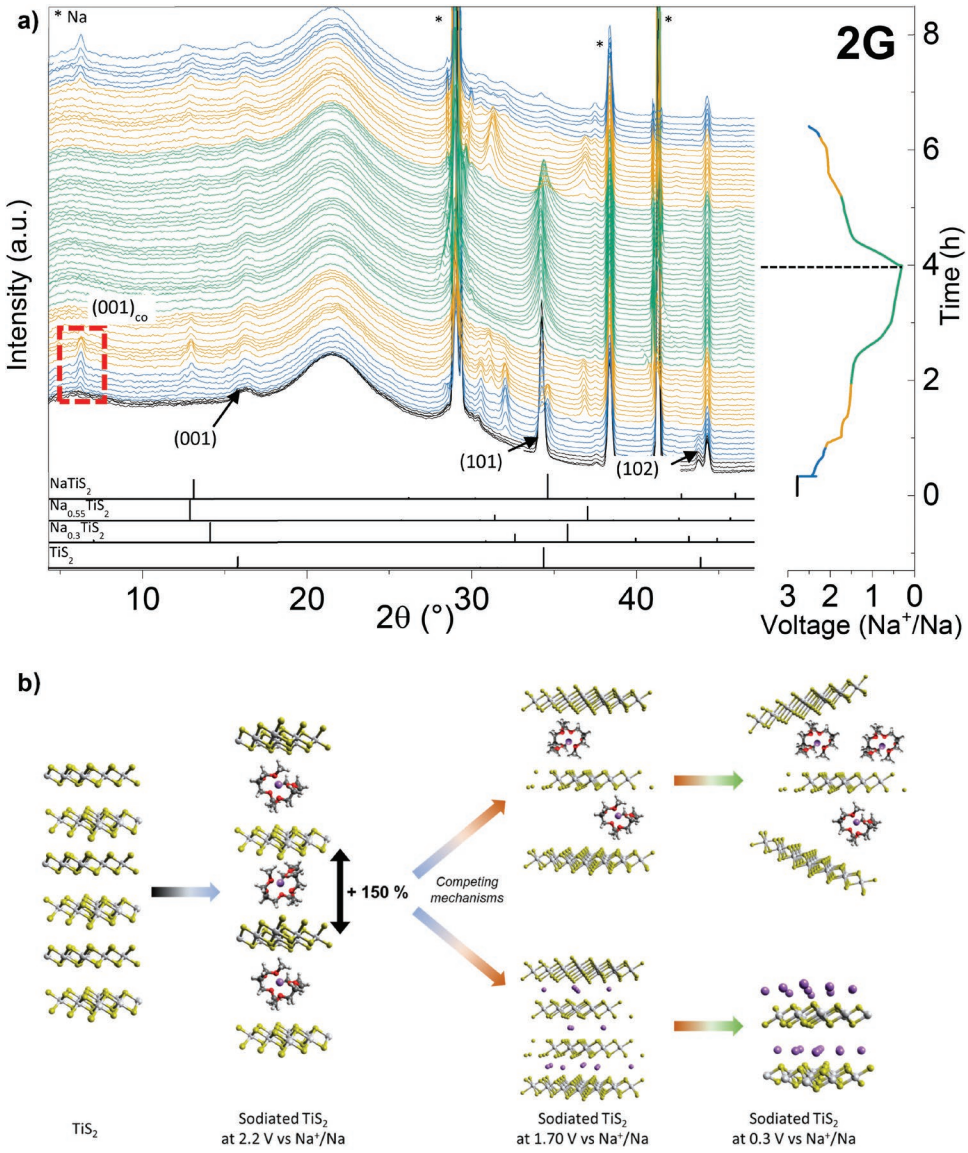

Figure 3. a) Voltage profiles at 100 mA g^{-1} with the corresponding operando diffraction patterns of the TiS_2 electrodes and the XRD patterns of standard data of $NaTiS_2$ (ICSD 26305), $Na_{0.55}TiS_2$ (ICSD 71092), $Na_{0.3}TiS_2$ (ICSD 201394), and TiS_2 (ICSD 52195); and b) schematic illustration of the mechanism during the sodiation process in 1 M $NaPF_6$ in 2G. Please note that the drawings for 1.70 and 0.3 V are just for the purpose of illustrating the increasing Na content. The exact crystal structure and atomic arrangement cannot be resolved due to the weak diffraction lines.

d-spacing to accommodate the Na^+ 2G system, see Figure S10, Supporting Information). We found that we could successfully fit the observed new features to this crystal structure, and that this leads to a corresponding change in lattice parameters from $a = b = 3.41$ and $c = 5.69$ for the parent TiS_2 to $a = b = 3.24$ and $c = 14.33$ for the expanded co-intercalation system. This corresponds to an expansion of the interlayer distance from 5.69 Å to 14.33 Å, which means an increase by 152% compared to the pristine electrode material. A comparable expansion was also observed by several authors for Li intercalation in TiS_2 with co-intercalation of PC,[16,21] and it is still significantly larger compared to the 24% observed for the EC:DEC and THF electrolytes (vide supra). The co-intercalation peaks remain at voltages above ≈1.70 V versus Na^+/Na. Such a large interlayer expansion is in line with the findings for solvent co-intercalation into graphite.[4a,5a] Zhuo et al. already reported on the expansion of the TiS_2 lattice based on their observation of the shift of the (001) peak from 15.6° to 12.5°–13.5° (2θ) at voltages ≈1.6 V versus Na^+/Na, which would correlate to an expansion by ≈15–25%.[15a] However, these measurements were performed over very narrow angular ranges (12°–15° (2θ) and 33°–38° (2θ)) which made a correct labeling of the peaks impossible. In fact, the peak at 12.5° (2θ) that they observed corresponded to the (002) plane. Similar misinterpretation of XRD data has been reported in other articles, where in situ and ex situ measurements have only been analyzed down to 22° (2θ).[10b] This shows that studying the storage behavior of the TiS_2 electrodes requires XRD measurements over a wider angular range,

in addition to analysis out of the preferred orientation plane. From these results it can be inferred that co-intercalation of 2G molecules is the only plausible explanation occurring at these voltage plateaus resulting in a large increase in interlayer distance. The SEM images displayed in Figure S11a–d, Supporting Information, corroborate the opening of the structure, which also appears to be wrinkled.

In addition, it can be seen that another new species arises during the second small voltage plateau around 2.1 V versus Na^+/Na, the onset of which coincides with the complete disappearance of the parent TiS_2 reflections. The new species has reflections at 12.8°, 31.2°, and 36.9° (2θ) which is consistent with the $Na_{0.55}TiS_2$ phase which was also detected in the case of the ED:DEC and THF electrolytes. However, in the case of 2G, its development was not obviously preceded by the formation of $Na_{0.3}TiS_2$. The $Na_{0.55}TiS_2$ phase disappears after the voltage plateau at 1.5 V versus Na^+/Na, and a further sodiation develops a single broad peak related to the $NaTiS_2$ (104) reflection at 34.2° (2θ). The breadth of the peak indicates that the crystallites are very small, and a complete pattern is therefore obscured. We do not detect the formation of Na_2S when fully sodiated at low voltages as seen by Tao et al.,[10b] however, in our case, our electrode material does not have a large amount of sulfur impurities. During desodiation, the $Na_{0.55}TiS_2$ signals at 31.1° and 36.9° (2θ) reappear with increased intensity relative to that observed during sodiation. However, the (003) reflection at 12.7° (2θ) is not observed, indicating that there may have been a rearrangement of the crystallites with respect to the incident X-Ray beam. Similarly, the reappearance of the (001) feature of the co-intercalated TiS_2 at 6.1° (2θ) occurs during desodiation at 2.25 V versus Na^+/Na, but is higher in intensity than was observed during the sodiation process, demonstrating certain reversibility of the reaction. At the same time, the other reflections at 30.4°, 32°, and 34.5° (2θ) also reappear, but with lower intensity than previously observed. Houdeville et al. already demonstrated in lithium the reversible attenuation of the (101) peak intensity during lithiation.[23] At the fully desodiated state, pristine TiS_2 is not observed to reform, and primarily co-intercalated species are observed from the operando measurements. Ex situ XRD measurements in Bragg-Brentano (reflection) geometry (see Figure S9, Supporting Information) show a very broad peak at 13.4° (2θ) that may be related to some very small Na_xTiS_2 crystallites that remain after desodiation.

This data indicates that there are two competing mechanisms that occur during sodiation: a conventional intercalation mechanism and an intercalation mechanism involving solvent co-intercalation. The co-existence of the two mechanisms is implicated in the initial stages of sodiation, where the clear co-intercalation features appear at 2.25 V versus Na^+/Na and appear unchanged until ≈1.70 V versus Na^+/Na. At the same time, there remain some reflections related to the parent TiS_2 that decay over time, and whose disappearance coincides with the formation of the $Na_{0.55}TiS_2$ phase at 2.0 V versus Na^+/Na (see orange color), indicating that these transitions are related and independent of the co-intercalation mechanism. As the peaks for co-intercalation reappear toward the end of the desodiation, the solvated ions remain in the system until the final stage of the desodiation. The fact that they are not observed at the voltages below 1.70 V versus Na^+/Na can be ascribed to an amorphization of the layer structure where the solvated ions are located. These two processes can be expected to have very different kinetics, and this mechanism is further discussed vide infra in the rate capability studies.

While we were only able to probe one cycle under operando conditions, we observed the reformation of the co-intercalated TiS_2 which indicates that the active material remains in an expanded state after desodiation. This is supported by post-mortem SEM images, which show that samples in the fully desodiated state preserve their layered structure, although they appear opened and expanded relative to the pristine structure (Figures S4b and S11e,f, Supporting Information). Ex situ XRD analysis in Bragg–Brentano geometry was also performed for the 60th cycle and compared to the 1st cycle in both sodiated and desodiated states, as can be seen in Figure S12, Supporting Information. Even though the co-intercalation peak intensities decreased over cycling, crystalline phases were still visible in the diffractogram. The broad peak located at around 13.4° (2θ) appeared in both the 1st and 60th cycles. This indicates that, despite the large lattice expansion, the layered structure does not delaminate and the structure is largely preserved over cycling. This is in line with what has been reported in case of co-intercalation of 2G into graphite.[17a]

2.3. Operando Electrochemical Dilatometry

While the XRD results provide clear evidence for a large expansion of the crystal lattice, operando electrochemical dilatometry (ECD) is a complementary method that can support such

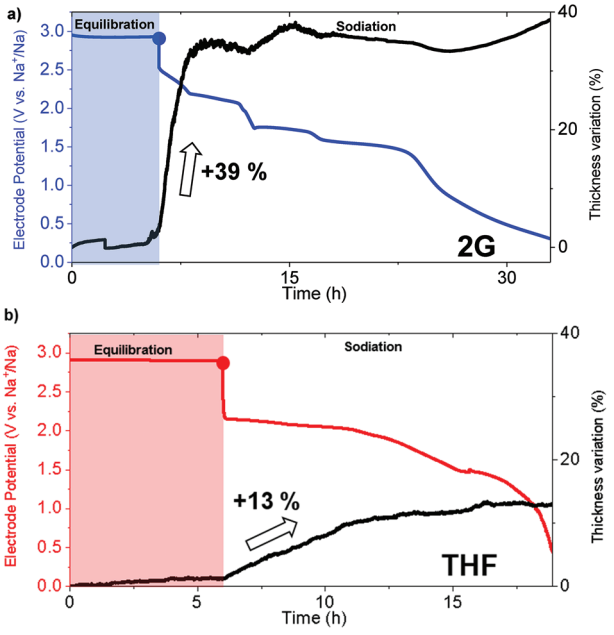

Figure 4. Operando electrochemical dilatometry measurements (3 electrode cell) of the TiS_2 electrodes at the first sodiation with: a) 1 M $NaPF_6$ in 2G at 45 μA cm^{-2} and b) 1 M $NaPF_6$ in THF at 90 μA cm^{-2}. The sudden and large increase in case of 2G indicates solvent co-intercalation during sodiation of TiS_2. Cells were equilibrated at open circuit voltage over several hours before starting the measurement. The beginning of the sodiation is marked by a dot.

findings,[18] which has been used to study the co-intercalation of 2G into graphite, for example.[17a] During an ECD experiment, the thickness change of an electrode is continuously measured during an electrochemical experiment.[18] Large volume changes in the crystal structure should also lead to notable changes in the thickness of the electrode. One significant difference from XRD is that it is also sensitive to changes in amorphous materials, as long as they lead to an appreciable change in electrode thickness. ECD results for the different electrolytes during the first sodiation are shown in **Figure 4** (2G, THF) and Figure S13, Supporting Information (EC:DEC). Overall, interpretation of the results were less straight-forward as compared to graphite (see ref. [17a]), however, some clear statements can be made. For the 2G electrolyte, the beginning of sodiation coincides with a rapid increase in electrode thickness (≈40%), which is well in line with the XRD results and the suggested co-intercalation of 2G at high voltages. Afterward, the thickness remains relatively constant until the end of discharge. Note that the change in electrode thickness (≈40%) is smaller compared to the change in interlayer distance (+152%) which is the result of having a particle electrode with open porosity that buffers the expansion. Much of the volume expansion therefore can take place within the electrode as also demonstrated for other materials.[22] In the case of THF and EC:DEC, for which only a small lattice expansion takes place (see XRD results in the previous section), the change in electrode thickness is notably smaller. In both electrolytes, the TiS_2 electrode expands during sodiation but the change remains below 15%.

2.4. Cycle Life

Long-term cycling was carried out to assess the durability of the TiS_2 electrode in the different electrolytes (**Figure 5** and Figure S14, Supporting Information). For all electrolytes, the discharge capacities (2nd cycle) are in the same range, that is, 260 mAh g^{-1} (2G), 270 mAh g^{-1} (THF), and 240 mAh g^{-1} (EC:DEC). The poorest cycle life was found for EC:DEC with almost 30% of capacity loss over 50 cycles, which is in accordance to the operando XRD results. A comparison of the different cycles in Figure 5d shows that the loss is largely linked to the disappearance of the upper plateau. The underlying process is unclear so far but might be rooted in decomposition reactions of the carbonates.[23] For 2G, a capacity increase over cycling is initially observed (see Figure 5b) which was also found in another study.[10b] After reaching a maximum capacity of 300 mAh g^{-1}, the capacity slowly fades, retaining ≈ 170 mAh g^{-1}

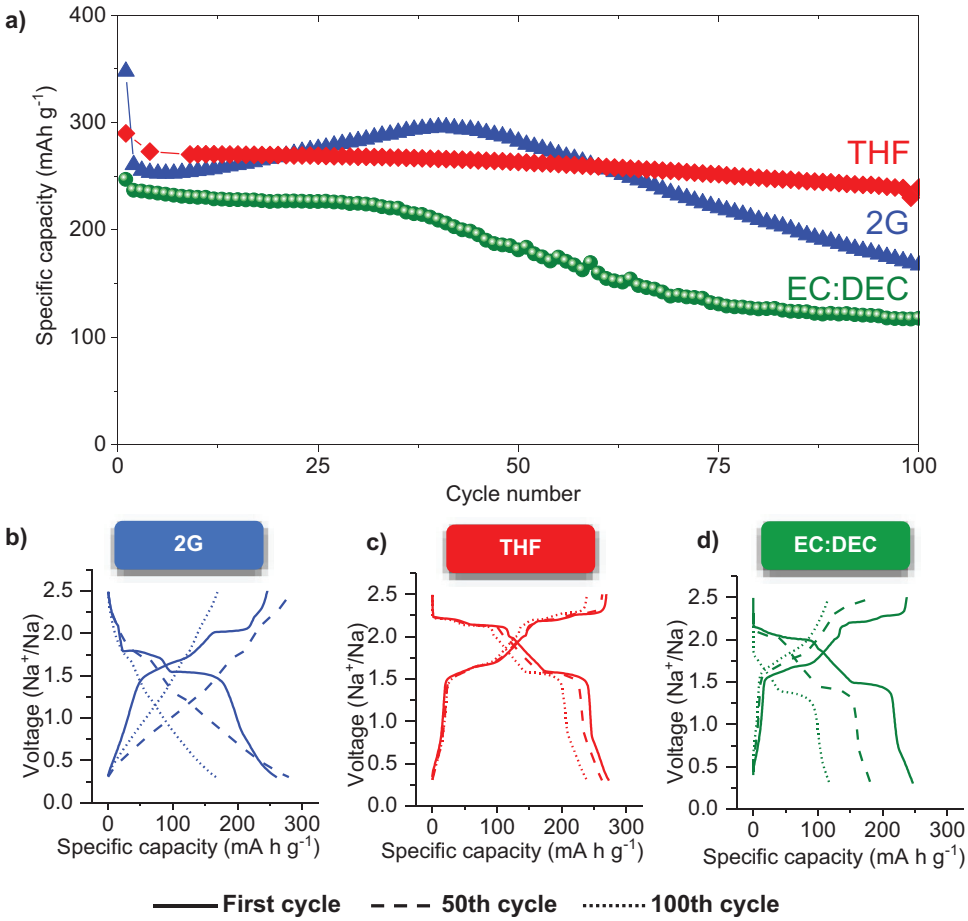

Figure 5. a) Long-term stability by using galvanostatic charge–discharge of TiS_2 electrodes at 100 mA g^{-1} in different electrolytes, and first, 50th and 100th cycle for: b) 1 M $NaPF_6$ in 2G, c) 1 M $NaPF_6$ in THF, and d) 1 M $NaPF_6$ in EC:DEC.

after 100 cycles (a 35% loss compared to the 2nd cycle). The voltage profiles shown in Figure 5b show that the voltage plateaus are lost over cycling and the storage mechanism behaves more like a solid solution-type mechanism, that is, the electrode potential changes continuously with the amount of sodium added/removed. Among all the electrolytes employed, THF exhibited the best cycle life. As can be seen, the cell retains 83% of its initial capacity in the first 100 cycles. In addition, the voltage profiles displayed no significant changes (see Figure 5c) and the plateaus remained unchanged. Finally, as displayed in Figure S14, Supporting Information, the Coulomb efficiency showed that the system is stable and reversible with cycling in the case of the 2G and THF solvent electrolytes.

Rate capability measurements were made between 0.01 and 2 A g^{-1} (see Figure S15, Supporting Information). In the case of THF and EC:DEC, increasing rates lead to decreasing capacities, which is well expected. For 2G, however, the situation is different, as the capacity remained largely constant at around 240 mAh g^{-1} between 0.01 and 0.5 A g^{-1}. At 0.5 A g^{-1} the values are much lower for the other solvents (150 and 175 for EC:DEC and THF, respectively, with THF overall showing a better rate capability than EC:DEC). We believe that this high-rate capability relates to the solvent co-intercalation which leads to a more opened, layered structure that facilitates ion-diffusion. This mechanism would be in line with reports on the fast ion diffusion of solvated ions in graphite.[17a,24] In fact, Jung et al. calculated that diffusion of solvated Na^+ in graphite can be faster compared to Li^+ diffusion.[6b]

2.5. Theoretical Considerations

The stark difference in electrochemical behavior exhibited by the different electrolytes could be caused by differences in the solvation shell of the sodium cation and the interactions between the cation and the solvents. The solvation shell structure of sodium has been investigated in many studies, and there is a consensus that the coordination number is between 5 and 7, but often found to be 6.[3f] Two 2G molecules are enough to satisfy this, while up to six THF or EC/DEC molecules are needed to form a complete solvation shell. We therefore used density functional theory to study complexes of the solvent molecules with Na^+ to estimate the stability and size of relevant solvation structures. The desolvation energy, a key parameter for solvent co-intercalation phenomenon,[25] shows that of the studied solvents 2G forms the most stable solvation shells (**Table 1**). Moreover, the 2G-based electrolytes produce by far the smallest solvation shell, with a radius of 4.2 Å as measured from the cation to the furthest hydrogen atom. TiS_2 is a layered structure and the interlayer distance is determined by the global minimum in the energy of the system. Therefore, there is an energetic cost to both increasing and decreasing the interlayer distance from that of the equilibrium distance. If, however, the energetic cost of expanding the lattice to accommodate a solvated ion is less than the cost of creating a bare ion at the electrolyte/electrode interface, co-intercalation should be more likely to occur. As the glyme-based electrolytes yield the smallest solvation shells, thus requiring less expansion of the lattice to

Table 1. The computed desolvation energies for single solvents, radius of the solvation shell as measured by the largest distance between the cation and any atom in the solvent, the desolvation energy per radius, and the desolvation energy per cross sectional area.

Solvent	Desolvation energy [kJ mol^{-1}]	Radius [Å]	Desolvation energy/radius [kJ mol^{-1} $Å^{-1}$]	Desolvation energy/cross-sectional area [meV $Å^{-2}$]
2G	123.5	4.2	29.4	23.1
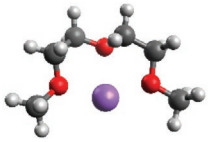				
THF	68.7	5.5	12.5	7.5
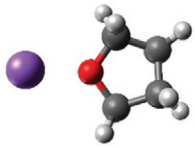				
EC	59.5	6.3	9.4	4.9
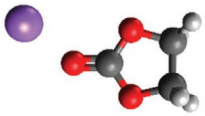				
DEC	46.8	6.2	7.5	4.0
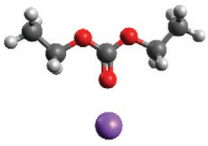				

accommodate a solvated ion, along with the largest desolvation energies, they are prime candidates to form ternary intercalation compounds. Comparing the ratios between desolvation energies and radii (see Table 1), this unified measure highlights the difference between the glymes and the other solvents. It is also noteworthy that the energetic cost of removing a single solvent molecule from the cation is quite large for 2G, compared with THF and EC:DEC (Table 1). Looking at the cross-sectional area of the solvation shells, we can calculate the desolvation energy per unit area and compare it to the interlayer binding energies per unit area as reported by Krogel et al.[26] The change in binding energy per unit area upon expansion is in the range of 20–30 meV $Å^{-2}$, thus diglyme with 23.1 meV $Å^{-2}$ is in this range, while the other solvents are far outside this range. This fully supports the solvent co-intercalation mechanism for 2G while desolvation would be more likely for the other solvents. In addition, it also fits with the evaluation of the kinetic capabilities of these systems, where in the 2G electrolyte the capacity remains almost completely unaffected by the applied current densities, until current densities reach 1 A g^{-1}.

2.6. Full Cells

In order to assemble a solvent co-intercalation battery, that is, a battery showing solvent co-intercalation at both the positive and negative electrode, two different electrodes need to be paired. Here, we assembled a CoIB based on graphite as the negative electrode (anode during discharge), sodiated TiS_2 as the positive electrode (cathode), and a diglyme-based electrolyte. **Figure 6** displays the three-electrode measurements of the full cell. Prior to operation, the electrodes were pre-cycled in their respective voltage ranges resulting in sodiated TiS_2 and desodiated graphite. The cell voltage was controlled between 2.1 and 0 V and both electrode potentials were monitored with respect to a sodium reference electrode. As can be observed, both graphite and TiS_2 showed their characteristic voltage plateaus at 1.75 and 1.55 V versus Na^+/Na in the case of TiS_2 and ≈0.5 V versus Na^+/Na in the case of graphite. The graphite electrode was oversized in order to exclude any Na plating from the beginning. In this setup, the graphite | TiS_2 CoIB is able to reach an energy density of ≈60 Wh kg^{-1} and a specific capacity of 55 mAh g^{-1} based in on the total mass of anode, cathode and sodium intercalated, corresponding to 0.66 mAh in absolute numbers. This value is close to the theoretical energy density (≈ 62 Wh kg^{-1}) calculated on the basis of the individual voltage ranges obtained in Figure 6 and it is superior to many advanced supercapacitors even in ionic liquid electrolytes.[27] At the same time, the energy density is small compared to LIBs or SIBs. The main reason for this is the low average voltage of the TiS_2 cathode which only allows an overall average cell voltage of around 1 V. It is clear that other materials and redox couples need to be found in order to achieve a higher energy density. Our study nevertheless represents the first proof-of-concept of a solvent co-intercalation battery. This new type of battery could fill the gap between traditional batteries and supercapacitors, a place inhabited by pseudocapacitive materials, hybrid supercapacitors, or dual batteries.[28]

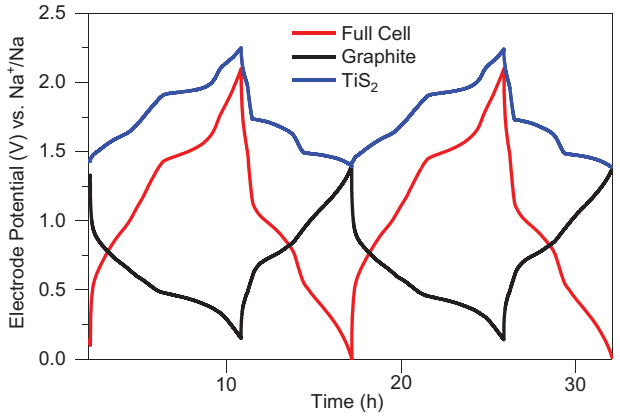

Figure 6. Voltage profiles in a three-electrode Swagelok set-up at 0.02 A $g^{-1}_{gcathode}$ with graphite as anode and TiS_2 as cathode materials in 1 M $NaPF_6$ in 2G.

3. Conclusion

Here, a comprehensive study on the effect of different sodium-ion electrolyte solvents on the electrochemical reaction mechanism with a layered transition metal dichalcogenide material, that is, TiS_2, was presented. Operando XRD and dilatometry showed that Na-diglyme complexes co-intercalate, like with graphite, into the TiS_2 active material. Solvent co-intercalation leads to a shift of the electrode's redox potential by around 350 mV, accompanied by a volume expansion as large as 150%. The charge storage is reversible providing 170 mAh g^{-1} after 100 cycles. In addition, TiS_2 does not revert back to its pristine state during charging but remains expanded. This means that the use of diglyme permanently modifies the structure. This is also seen from the voltage profiles which show (over 100 cycles) a continuous change from a two-step behavior to a sloping behavior. No signs for solvent co-intercalation are found for THF and EC:DEC. In this case, the sodiation of the TiS_2 electrodes results in the formation of different Na_xTiS_2 compounds. DFT calculations support the experimental findings observed, showing that diglyme forms a very small and stable solvation shell around Na^+ making the complete solvation complex more likely to co-intercalate. With TiS_2 being identified as a "co-intercalation electrode", the first solvent co-intercalation battery was assembled by pairing TiS_2 (positive electrode) with graphite (negative electrode). Due to the low average voltage of around 1 V, the energy density so far is limited to around 60 Wh kg^{-1}. We are still in an early stage to understand the potential benefits of solvent co-intercalation for practical batteries. However, the advantage of such a battery concept is that the overpotentials caused by the stripping of solvation shells can be minimized or avoided. This could enable the development of highly energy efficient batteries with minimum charge transfer resistance and improved low temperature performance (where the charge transfer can become rate limiting). The same approach could could also be utilized for multi-valent ion cell chemistries which typically suffer from very strong desolvation energies.

4. Experimental Section

Electrode Preparation: The electrodes consisted of 70 wt% titanium sulfide powder, 200 mesh, 99.9% (Sigma Aldrich), 20 wt% conductive additive (Super P), and 10 wt% PVDF binder (poly(vinylidene difluoride) from PI-KEM Ltd). NMP (N-methylpyrrolidone from Sigma-Aldrich) was used as solvent to form the slurries that were cast onto carbon coated aluminum current collectors. The electrode sheets were dried at room temperature overnight, punched into electrodes, and dried again under vacuum overnight at 110 °C. The electrode preparation was performed in an argon filled glovebox from MBraun ($H_2O < 0.1$ ppm, $O_2 < 0.1$ ppm). The mass loading of the electrodes was ≈5 mg cm^{-2}.

Electrochemical Measurements: All cell assembly took place in an argon filled glovebox from MBraun ($H_2O < 0.1$ ppm, $O_2 < 0.1$ ppm). Film thicknesses were measured inside the glovebox before cell assembly using a digital thickness dial gauge from Käfer Messuhrenfabrik GmbH.

For galvanostatic cycling, CR2032 coin cells (MTI Corp.) were assembled with electrodes of 12 mm diameter. Na metal (BASF) was used as the counter electrode and a Whatman membrane (GF/A) as the separator with 100 µL of electrolyte.

For the electrolyte preparation, sodium hexafluorophosphate ($NaPF_6$, purity > 99%, Alfa Aesar) was pre-dried overnight at 100 °C in a Büchi oven under vacuum. Diglyme (2G, Sigma Aldrich), tetrahydrofuran (THF, Sigma Aldrich), ethylene carbonate (EC, Sigma Aldrich), and diethyl carbonate (DEC, Sigma Aldrich) were pre-dried on 4 Å porous molecular sieves overnight.

Electrochemical galvanostatic charge–discharge experiments were conducted on a Biologic BCS 805 battery cycler with a voltage window of 0.3–2.5 V versus Na^+/Na at various current densities. Preliminary experiments demonstrated that a cut-off voltage of 0.3 V is the optimum for achieving stable electrochemical performance.

Full cells were fabricated by taking graphite as anode and TiS_2 as cathode with 2G-based electrolyte. Before assembly, the graphite electrodes were activated by cycling with metallic sodium between 2 and 0.01 V and left in the desodiated state. Similarly, the TiS_2 electrodes were also activated between 2.5 and 0.3 V until fully sodiated. Full cells were then assembled with the activated electrodes with glass fiber separators soaked with 150 µL of the electrolyte.

Physicochemical Characterization: The cross-sectional images of the electrodes were taken with a PhenomProX scanning electron microscope (SEM) from ThermoFisher with an accelerating voltage of 5 kV. Cross-sectional samples were prepared by cutting electrodes with scissors and using vertical sample holders.

Ex situ XRD measurements were made by using a D2 Phaser XRD from Bruker with Cu Kα radiation (λ = 0.15406 nm, 30 kV, 10 mA) between 5° and 80° (2θ), using a step width of 0.02°. Electrodes for XRD measurements were extracted from disassembled cells in an Ar-filled glovebox and measured in air-tight sample holders with a low-intensity Si background in order to maintain an inert (Ar) atmosphere during measurement.

Operando electrochemical XRD experiments were performed by cycling electrodes in an in-house built two-electrode cell in transmission geometry with 23 µm thick Mylar windows using a GaIn Excillum MetalJet X-ray source (Ga-Kα, 9.2 keV) operating at 160 kV with a Pilatus3 S 1 M area detector. Measurements were carried out in the X-Ray Core Lab operated by the Helmholtz-Zentrum Berlin für Materialien und Energie, GmbH. The obtained 2D images were radially integrated and referenced to LaB_6. A 10 mm diameter TiS_2 electrode was employed as the working electrode and 10 mm sodium was used as the counter electrode with 100 µL of electrolyte. The structural changes of the electrodes were measured continuously during the electrochemical galvanostatic charge–discharge experiments with a Biologic SP-150 potentiostat between 0.3 and 2.5 V versus Na^+/Na at 100 mA g^{-1}. For simplicity of comparison, all reported operando XRD data have been converted to equivalent angles (2θ) for Cu Kα radiation.

Operando electrochemical dilatometry experiments were conducted in an ECD-nano device from EL-CELL, GmbH. The cell is designed in a three-electrode configuration. Working (10 mm) and counter electrodes were separated by a fixed glass ceramic separator, which guaranteed that only the thickness change of the working electrode was measured. Na metal was used as the reference electrode and the electrolyte volume was ≈250 µL. The thickness change of the electrodes was measured simultaneously during electrochemical galvanostatic charge–discharge experiments.

The relative thickness change (%) was calculated according the following equation:

$$h_{\text{relative}}(\%) = \frac{h_n}{h_0} \times 100 \quad (1)$$

where h_0 is the initial thickness (after 4 h at OCV) of the electrode without the thickness of the current collector, and h_n is the electrode thickness at each point without the thickness of the current collector.

Density Functional Theory: The Gaussian 16 suite was used at the M062X/6-311++G(d,p) level of theory to optimize the structure of the isolated solvent molecules (2G, THF, EC, and DEC), their structures and energies upon coordination with Na^+, and individual Na^+.[29] A frequency calculation was carried out on the optimized structures to ensure they represented local minima in the energy landscape, and the thermally corrected energies were used to compute the energies of solvation/desolvation according to:

$$E = E_{Na} + nE_{\text{solv}} - E_{\text{complex}} \quad (2)$$

where E_{complex}, E_{solv}, and E_{Na} are the thermally corrected energies of the Na^+-solvent complex, the single solvent, and Na^+, respectively, and n is the number of solvent molecules in the complex. In all calculations the implicit solvent model SMD was used to mimic the dielectric environment of the systems, with dielectric constants set to that of the solvents under investigation (ε = 7.2, ε = 7.6, ε = 89.78, ε = 2.805 for 2G, THF, EC, DEC, respectively).[30] The single sodium cation Na^+ was optimized in an implicit solvent environment using each of the four values of the dielectric constant.

Supporting Information

Supporting Information is available from the Wiley Online Library or from the author.

Acknowledgements

This project received funding from the European Research Council (ERC) under the European Union's Horizon 2020 research and innovation programme (grant agreement No. [864698], SEED). The authors thank the Helmholtz-Zentrum Berlin für Materialien und Energie for the allocation of the Excillum MetalJet X-ray source for the operando electrochemical XRD experiments. The authors also thank Dr. Roland Mainz from Helmholtz-Zentrum Berlin für Materialien und Energie, GmbH for assistance during the operando XRD experiments.

Open access funding enabled and organized by Projekt DEAL.

Conflict of Interest

The authors declare no conflict of interest.

Data Availability Statement

The data that support the findings of this study are available from the corresponding author upon reasonable request.

Keywords

co-intercalation batteries, operando X-ray diffraction, sodium-ion batteries, solvent co-intercalation, titanium disulfide

Received: July 13, 2022
Revised: September 23, 2022
Published online: October 21, 2022

[1] a) M. Armand, J.-M. Tarascon, *Nature* **2008**, *451*, 652; b) G. E. Blomgren, *J. Electrochem. Soc.* **2016**, *164*, A5019.

[2] a) D. Kundu, E. Talaie, V. Duffort, L. F. Nazar, *Angew. Chem., Int. Ed.* **2015**, *54*, 3431; b) C. Vaalma, D. Buchholz, M. Weil, S. Passerini, *Nat. Rev. Mater.* **2018**, *3*, 18013; c) I. Hasa, S. Mariyappan, D. Saurel, P. Adelhelm, A. Y. Koposov, C. Masquelier, L. Croguennec, M. Casas-Cabanas, *J. Power Sources* **2021**, *482*, 228872; d) N. Tapia-Ruiz, A. R. Armstrong, H. Alptekin, M. A. Amores, H. Au, J. Barker, R. Boston, W. R. Brant, J. M. Brittain, Y. Chen, M. Chhowalla, Y.-S. Choi, S. I. R. Costa, M. Crespo Ribadeneyra, S. A. Cussen, E. J. Cussen, W. I. F. David, A. V. Desai, S. A. M. Dickson, E. I. Eweka, J. D. Forero-Saboya, C. P. Grey, J. M. Griffin, P. Gross, X. Hua, J. T. S. Irvine, P. Johansson, M. O. Jones, M. Karlsmo, E. Kendrick, et al., *J. Phys.: Condens. Matter* **2021**, *3*, 031503; e) C. Delmas, *Adv. Energy Mater.* **2018**, *8*, 1703137.

[3] a) S. P. Ong, V. L. Chevrier, G. Hautier, A. Jain, C. Moore, S. Kim, X. Ma, G. Ceder, *Energy Environ. Sci.* **2011**, *4*, 3680; b) P. K. Nayak, L. Yang, W. Brehm, P. Adelhelm, *Angew. Chem., Int. Ed.* **2018**, *57*, 102; c) S. Komaba, *Chem. Lett.* **2020**, *49*, 1507; d) R. Usiskin, Y. Lu, J. Popovic, M. Law, P. Balaya, Y.-S. Hu, J. Maier, *Nat. Rev. Mater.* **2021**, *6*, 1020; e) P. Adelhelm, P. Hartmann, C. L. Bender, M. Busche, C. Eufinger, J. Janek, *Beilstein J. Nanotechnol.* **2015**, *6*, 1016; f) G. Åvall, J. Mindemark, D. Brandell, P. Johansson, *Adv. Energy Mater.* **2018**, *8*, 1703036.

[4] a) B. Jache, P. Adelhelm, *Angew. Chem.* **2014**, *126*, 10333; b) O. Lenchuk, P. Adelhelm, D. Mollenhauer, *Phys. Chem. Chem. Phys.* **2019**, *21*, 19378.

[5] a) B. Jache, J. O. Binder, T. Abe, P. Adelhelm, *Phys. Chem. Chem. Phys.* **2016**, *18*, 14299; b) M. Goktas, C. Bolli, J. Buchheim, E. J. Berg, P. Novák, F. Bonilla, T. f. Rojo, S. Komaba, K. Kubota, P. Adelhelm, *ACS Appl. Mater. Interfaces* **2019**, *11*, 32844; c) E. Goikolea, V. Palomares, S. Wang, I. R. de Larramendi, X. Guo, G. Wang, T. Rojo, *Adv. Energy Mater.* **2020**, *10*, 2002055; d) H. Kim, J. Hong, G. Yoon, H. Kim, K.-Y. Park, M.-S. Park, W.-S. Yoon, K. Kang, *Energy Environ. Sci.* **2015**, *8*, 2963; e) Y. Li, Y. Lu, P. Adelhelm, M.-M. Titirici, Y.-S. Hu, *Chem. Soc. Rev.* **2019**, *48*, 4655; f) J. Park, Z.-L. Xu, K. Kang, *Front. Chem.* **2020**, *8*, 432.

[6] a) M. Goktas, C. Bolli, J. Buchheim, E. J. Berg, P. Novák, F. Bonilla, T. Rojo, S. Komaba, K. Kubota, P. Adelhelm, *ACS Appl. Mater. Interfaces* **2019**, *11*, 32844; b) S. C. Jung, Y.-J. Kang, Y.-K. Han, *Nano Energy* **2017**, *34*, 456; c) A. P. Cohn, K. Share, R. Carter, L. Oakes, C. L. Pint, *Nano Lett.* **2016**, *16*, 543.

[7] a) K. Xu, A. von Cresce, U. Lee, *Langmuir* **2010**, *26*, 11538; b) S. S. Zhang, K. Xu, T. R. Jow, *J. Power Sources* **2003**, *115*, 137; c) T. R. Jow, M. B. Marx, J. L. Allen, *J. Electrochem. Soc.* **2012**, *159*, A604.

[8] a) Q. Yun, L. Li, Z. Hu, Q. Lu, B. Chen, H. Zhang, *Adv. Mater.* **2020**, *32*, 1903826; b) Y. Zhang, Q. Zhou, J. Zhu, Q. Yan, S. X. Dou, W. Sun, *Adv. Funct. Mater.* **2017**, *27*, 1702317; c) R. Sahoo, M. Singh, T. N. Rao, *ChemElectroChem* **2021**, *8*, 2358.

[9] H.-S. Ryu, J.-S. Kim, J.-S. Park, J.-W. Park, K.-W. Kim, J.-H. Ahn, T.-H. Nam, G. Wang, H.-J. Ahn, *J. Electrochem. Soc.* **2012**, *160*, A338.

[10] a) A. Chaturvedi, E. Edison, N. Arun, P. Hu, C. Kloc, V. Aravindan, S. Madhavi, *ChemistrySelect* **2018**, *3*, 524; b) H. Tao, M. Zhou, R. Wang, K. Wang, S. Cheng, K. Jiang, *Adv. Sci.* **2018**, *5*, 1801021.

[11] a) F. Flamary-Mespoulie, A. Boulineau, H. Martinez, M. R. Suchomel, C. Delmas, B. Pecquenard, F. L. Cras, *Energy Storage Mater.* **2020**, *26*, 213; b) D. Y. Oh, Y. E. Choi, D. H. Kim, Y.-G. Lee, B.-S. Kim, J. Park, H. Sohn, Y. S. Jung, *J. Mater. Chem. A* **2016**, *4*, 10329.

[12] L. Wang, J. Zou, S. Chen, G. Zhou, J. Bai, P. Gao, Y. Wang, X. Yu, J. Li, Y.-S. Hu, H. Li, *Energy Storage Mater.* **2018**, *12*, 216.

[13] D. S. Tchitchekova, A. Ponrouch, R. Verrelli, T. Broux, C. Frontera, A. Sorrentino, F. Bardé, N. Biskup, M. E. Arroyo-de Dompablo, M. R. Palacín, *Chem. Mater.* **2018**, *30*, 847.

[14] X. Sun, P. Bonnick, L. F. Nazar, *ACS Energy Lett.* **2016**, *1*, 297.

[15] a) S. Zhuo, G. Huang, Y. Lei, W. Wang, Z. Liu, X. Xu, J. Yin, H. N. Alshareef, *Small Methods* **2020**, *4*, 2000439; b) Z. Hu, Z. Tai, Q. Liu, S. W. Wang, H. Jin, S. Wang, W. Lai, M. Chen, L. Li, L. Chen, *Adv. Energy Mater.* **2019**, *9*, 1803210; c) Y. Liu, H. Wang, L. Cheng, N. Han, F. Zhao, P. Li, C. Jin, Y. Li, *Nano Energy* **2016**, *20*, 168.

[16] a) J. Dahn, M. Py, R. Haering, *Can. J. Phys.* **1982**, *60*, 307; b) R. Schöllhorn, in *Intercalation Chemistry* (Eds: M. S. Whittingham, A. J. Jacobson), Academic Press, USA **1982**, p. 315.

[17] a) M. Goktas, C. Bolli, E. J. Berg, P. Novák, K. Pollok, F. Langenhorst, M. v. Roeder, O. Lenchuk, D. Mollenhauer, P. Adelhelm, *Adv. Energy Mater.* **2018**, *8*, 1702724; b) I. Escher, Y. Kravets, G. A. Ferrero, M. Goktas, P. Adelhelm, *Energy Technol.* **2021**, *9*, 2000880.

[18] I. Escher, M. Hahn, G. A. Ferrero, P. Adelhelm, *Energy Technol. 10*, 2101120.

[19] P. Hu, B. Wang, D. Xiao, K. Aifantis, *Nano Energy* **2019**, *63*, 103820.

[20] E. A. Suslov, O. V. Bushkova, E. A. Sherstobitova, O. G. Reznitskikh, A. N. Titov, *Ionics* **2016**, *22*, 503.

[21] R. G. Houdeville, A. P. Black, A. Ponrouch, M. R. Palacín, F. Fauth, *J. Electrochem. Soc.* **2021**, *168*, 030514.

[22] a) W. Brehm, A. L. Santhosha, Z. Zhang, C. Neumann, A. Turchanin, M. Seyring, M. Rettenmayr, J. R. Buchheim, P. Adelhelm, *J Power Sources* **2020**, *6*, 100031; b) T. Palaniselvam, M. Goktas, B. Anothumakkool, Y.-N. Sun, R. Schmuch, L. Zhao, B.-H. Han, M. Winter, P. Adelhelm, *Adv. Funct. Mater.* **2019**, *29*, 1900790; c) T. Schott, J. L. Gómez-Cámer, P. Novák, S. Trabesinger, *J. Electrochem. Soc.* **2016**, *164*, A190.

[23] a) Y. Lee, J. Lee, H. Kim, K. Kang, N.-S. Choi, *J. Power Sources* **2016**, *320*, 49; b) S. Komaba, W. Murata, T. Ishikawa, N. Yabuuchi, T. Ozeki, T. Nakayama, A. Ogata, K. Gotoh, K. Fujiwara, *Adv. Funct. Mater.* **2011**, *21*, 3859.

[24] H. Kim, J. Hong, Y.-U. Park, J. Kim, I. Hwang, K. Kang, *Adv. Funct. Mater.* **2015**, *25*, 534.

[25] G. Yoon, H. Kim, I. Park, K. Kang, *Adv. Energy Mater.* **2017**, *7*, 1601519.

[26] J. T. Krogel, S. F. Yuk, P. R. C. Kent, V. R. Cooper, *J Phys Chem A* **2020**, *124*, 9867.

[27] Q. Dou, H. S. Park, *Energy Environ. Mater.* **2020**, *3*, 286.

[28] a) P. Cai, K. Zou, X. Deng, B. Wang, M. Zheng, L. Li, H. Hou, G. Zou, X. Ji, *Adv. Energy Mater.* **2021**, *11*, 2003804; b) J. M. Wrogemann, S. Künne, A. Heckmann, I. A. Rodríguez-Pérez, V. Siozios, B. Yan, J. Li, M. Winter, K. Beltrop, T. Placke, *Adv. Energy Mater.* **2020**, *10*, 2070033.

[29] a) M. J. Frisch, G. W. Trucks, H. B. Schlegel, G. E. Scuseria, M. A. Robb, J. R. Cheeseman, G. Scalmani, V. Barone, G. A. Petersson, H. Nakatsuji, X. Li, M. Caricato, A. V. Marenich, J. Bloino, B. G. Janesko, R. Gomperts, B. Mennucci, H. P. Hratchian, J. V. Ortiz, A. F. Izmaylov, J. L. Sonnenberg, F. D. Williams, F. Lipparini, F. Egidi, J. Goings, B. Peng, A. Petrone, T. Henderson, D. Ranasinghe, V. G. Zakrzewski, et al., Gaussian, Inc., Wallingford, CT **2016**; b) Y. Zhao, D. G. Truhlar, *Theor. Chem. Acc.* **2008**, *120*, 215.

[30] a) A. V. Marenich, C. J. Cramer, D. G. Truhlar, *J. Phys. Chem. B* **2009**, *113*, 6378; b) K. Xu, *Chem. Rev.* **2004**, *104*, 4303.